Research Article

Journal of RAMAN SPECTROSCOPY

Received: 8 February 2009 Accepted: 27 June 2009 Published online in Wiley Interscience: 15 September 2009

(www.interscience.wiley.com) DOI 10.1002/jrs.2407

Polar phonon mode selection rules in tip-enhanced Raman scattering

Samuel Berweger and Markus B. Raschke*

We discuss the use of the symmetry selectivity of phonon Raman scattering to determine nanocrystallographic information of solids using tip-enhanced Raman scattering (TERS). The necessary degrees of freedom arise from the combination of the Raman selection rules reflecting crystal symmetry superimposed by the polarization and *k*-vector-dependent field enhancement and scattering of the scanning probe tip. The resulting phonon TERS selection rules are discussed, including the use of the crystal Raman tensor and momentum conservation for polar phonon modes. We demonstrate the selection rules for both far-field and tip-enhanced near-field Raman scattering from bulk and nanocrystalline $LiNbO_3$.

Keywords: tip-enhanced Raman scattering; optical phonons; selection rules $LiNbO_3$

Introduction

Through the direct interaction with zone-center optical phonons, Raman scattering of crystalline solids can directly probe phonon resonances and their lifetimes.[1,2] As a result, Raman scattering has proven indispensable for the study of crystalline solids, providing insight into, for example, stress,[3] doping, electron–phonon coupling,[4,5] and phase transitions.[6,7] Furthermore, with the Raman tensor-based selection rules reflecting the crystal symmetry, Raman scattering allows the determination of crystallographic orientation.[8,9]

The desire for simultaneous spatial resolution in Raman scattering has resulted in the successful implementation in a confocal microscopy configuration. However, the commonly used epi-illumination and detection geometry with *k*-vectors normal with respect to sample surface reduces the available degrees of freedom. This limits the capability to probe crystal symmetry in general, and the spatial resolution is diffraction limited.

With tip-enhanced Raman scattering (TERS), the spatial resolution can be extended into the nanometer range. Drawing on the confinement and enhancement of both the incident and scattered electromagnetic field provided by the nanoscopic apex of a plasmonic scanning probe tip, nanometer spatial resolution[10] and single-molecule sensitivity[11–13] have been achieved. The technique has been successfully used to study molecular adsorbates,[11–13] carbon nanotubes,[10,14] and biomolecules[15,16] (see also, e.g., Refs. [17–19] for reviews and references therein). Although having been used in a specific tip-enhanced geometry to maximize the near-field contrast from crystalline materials,[20,21] a general description of the symmetry selectivity of the Raman response in TERS has not yet been developed.

Here, we illustrate that the photon–phonon momentum conservation underlying nano-Raman scattering from polar phonon modes[22] offers the potential to regain the necessary degrees of freedom that are lost in traditional far-field Raman microscopy, to probe the crystalline symmetry of a material even on the nanoscale. The application of TERS for the study of crystals exhibiting polar phonon modes then allows the identification of the crystallographic orientation of nanocrystals or the nanodomain topology of bulk materials as we have recently demonstrated for nanocrystalline $BaTiO_3$.[23] The method is generally applicable to a wide range of technologically relevant substances of reduced crystal symmetry (i.e. non-centrosymmetric) including those exhibiting piezoelectricity,[24] optical birefringence, nonlinear optical properties,[25] and correlated electron systems. We discuss the Raman selection rules, including the Raman tensor and crystal symmetry, and the role of momentum conservation as it applies to phonon propagation direction and quasi-modes. These considerations provide the basis for the overall selection rules as they apply in a tip-enhanced geometry, arising from the superposition of the polarization-dependent enhancement and scattering of the tip, and the general Raman selection rules. We demonstrate the applications of the selection rules both in the far-field and their extension to the tip-enhanced near-field case.

As a model system, we use lithium niobate ($LiNbO_3$), which has an indirect bandgap of ~4 eV. As a result of its transparency through the near-UV to mid-IR spectral region, it has found widespread use in optical waveguides and electro-optic modulators.[26,27] The large second-order nonlinear susceptibility has further rendered it suitable for a wide variety of nonlinear optical applications including frequency doubling[28] and optical parametric generation.[29] Comparably large Raman scattering cross sections[30] have also made it a viable candidate for Raman lasers.[31]

$LiNbO_3$ exhibits trigonal symmetry, with a ferroelectric lattice distortion along the optical *c*-axis. The crystal structure is shown schematically in Fig. 1(a). With two formula units per unit cell, there are 27 optical vibrational modes, 13 of which are Raman active.[24] The large Raman cross section in combination with the uniaxial crystal structure makes it a suitable model system to illustrate the phonon Raman selection rules of TERS for the study of crystalline order.

* *Correspondence to: Markus B. Raschke, Department of Chemistry, University of Washington, Seattle, WA 98195, USA. E-mail: raschke@chem.washington.edu*

Department of Chemistry, University of Washington, Seattle, WA 98195, USA

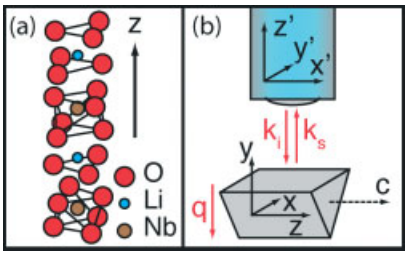

Figure 1. (a) Illustration of the uniaxial crystal structure of $LiNbO_3$ along the optical *z*-axis. (b) Geometry of the far-field Raman spectroscopy setup used for reference, with optical and phonon wavevectors indicated. Incident light is focused onto a bulk $LiNbO_3$ single-crystal wafer by means of a NA = 0.1 objective. The backscattered Raman signal is collected through the same objective and spectrally resolved using a grating spectrometer with a N_2(l)-cooled CCD. The lab frame is fixed through all measurements while the crystal is rotated.

General Raman Selection Rules

We begin by discussing the general far-field Raman selection rules. They reflect the crystal symmetry and thus allow one to determine crystallographic orientation. Specific results for $LiNbO_3$ will be presented below.

In the far-field, the induced optical polarization at the Raman-shifted frequency for the *n*-th phonon mode is given by $P_{j,n} \propto \chi_{jk,n} E_k^{inc}$ ($j, k = x, y, z$) with the Raman tensor $\chi_{jk,n}$, and electric field of the incident light E_k^{inc}. Because the Raman tensor reflects the crystal symmetry, the observation (or absence) of modes in a given scattering geometry may allow the complete determination of crystal symmetry and crystal orientation. However, this information may be insufficient, in particular if the incident or scattered polarizations or incident and scattered wavevectors do not coincide with one of the principal crystallograpic axes. Additional information regarding the crystallographic orientation may be gained by considering those Raman active modes that exhibit a dependence of the Raman shift on the phonon propagation direction.

Raman active phonon modes are either polar or nonpolar.[22] For polar modes, the atomic displacement induces an electric dipole moment, and the corresponding modes are therefore also infrared active. Nonpolar phonon modes exhibit a Raman shift independent of the phonon propagation direction. For polar phonon modes, the macroscopic electric field associated with the phonon oscillation leads to an increase of the atomic restoring force experienced by the phonons propagating along the phonon polarization direction $\boldsymbol{\xi}$. As a result, the energy of a phonon propagating perpendicular to its polarization direction (transverse optical, TO) is lower than that of the corresponding phonon propagation parallel to the phonon polarization direction (longitudinal optical, LO). This gives rise to the energy splitting between the TO and LO modes.[32]

The phonon wavevector $\boldsymbol{q}$, and therefore the propagation direction, can be determined from momentum conservation of the wavevectors of the incident $\boldsymbol{k_i}$ and scattered $\boldsymbol{k_s}$ light: $\boldsymbol{q} = \boldsymbol{k_i} - \boldsymbol{k_s}$. If $\boldsymbol{q} \parallel \boldsymbol{\xi}$, the LO mode is excited, whereas for $\boldsymbol{q} \perp \boldsymbol{\xi}$, the TO mode is active. Hence, for a given polar phonon mode, the polarization and *k*-vector-selective observation of the TO or LO modes provide insight into the crystallographic orientation.

For optical excitation of a crystalline sample of unknown orientation, the resulting optical phonon propagation direction may not coincide with one of the principal axes of the crystal. The exact behavior in such a case depends on the structural details of the crystal considered. For simplicity, but without loss of generality, the following discussion focuses on crystals where long range-electrostatic forces dominate over the local anisotropy of the lattice (i.e. the TO–LO energy splitting is larger than the A_1–E splitting),[32] as is the case for $LiNbO_3$.[34]

The frequency of phonons propagating at an angle θ with respect to the principal *z*-axis in $LiNbO_3$ can then be described to a good approximation by:[32]

$$\omega_{LO}^2 = \omega_{A_1^{LO}}^2 \cos^2(\theta) + \omega_{E^{LO}}^2 \sin^2(\theta)$$
$$\omega_{TO}^2 = \omega_{A_1^{TO}}^2 \sin^2(\theta) + \omega_{E^{TO}}^2 \cos^2(\theta)$$

It can be seen that if the phonon propagation direction is not along one of the principal axes, the phonon is of a mixed character and the spectral positions of the resulting so-called quasi-modes yield information about the crystallographic orientation with respect to the phonon propagation direction. In contrast, for a phonon propagating in the *x*-*y* plane, no mode mixing occurs. Rather, with a component of the phonon propagation direction along both the *x*- and *y*-axes, this enables the simultaneous observation of both the E^{TO} and E^{LO} modes if polarization conditions due to the corresponding Raman tensor are met.

The discussion above illustrates how the far-field Raman selection rules will allow the determination of crystallographic orientation. In considering a corresponding phonon TERS response from nanocrystals, we must also account for the symmetry-selective enhancement and scattering of the incident and scattered light by the tip. As a result of the ∞mm tip symmetry, light polarized parallel with respect to the tip axis (p-polarized) is predominantly enhanced compared with perpendicular (s-polarized) excitation. This can be expressed through the field enhancement factors F_u^{inc} and F_v^{scat}, where *u* and *v* denote the polarization state of the incident and scattered light, respectively. In general, $F_p > F_s$, with details depending on the nature of the tip plasmon, amount of Raman shift, and exact influence of the tip geometry on the polarization state of the incident and scattered light,[35,36] as will be discussed further below. The induced polarization at the Raman-shifted frequency can then be written as $P_{j,n} \propto F_v^{scat} \chi_{jk,n} F_u^{inc} E_k^{inc}$. This is analogous to the treatment of the optical response from a planar interface considering the Fresnel factor for the fields.[37] The field enhancement factors for the tip can be contracted approximately into a single tensor that takes, for example, for the specific lab frame shown in Fig. 2(a), the following form:

$$\mathcal{F}_{vu}^{TERS} = F_v^{scat} F_u^{inc} = \begin{pmatrix} F_{ss} & F_{sp} & 0 \\ F_{ps} & F_{pp} & 0 \\ 0 & 0 & 0 \end{pmatrix}$$

As a result, the tip-enhanced and scattered Raman intensity is given by $I_{scat} \propto |\mathcal{F}_{vu} \chi_{jk,n} E_k^{inc}|^2$.

The discussion above shows that when considering the polarization-dependent tip enhancement and scattering together with the Raman selection rules, from a polarization-dependent study of phonon TERS spectra, the crystalline orientation of a material may be determined with nanometer spatial resolution.

In contrast to molecular systems, comparably small Raman cross sections abound for crystalline materials. This is the result of the

Journal of RAMAN SPECTROSCOPY

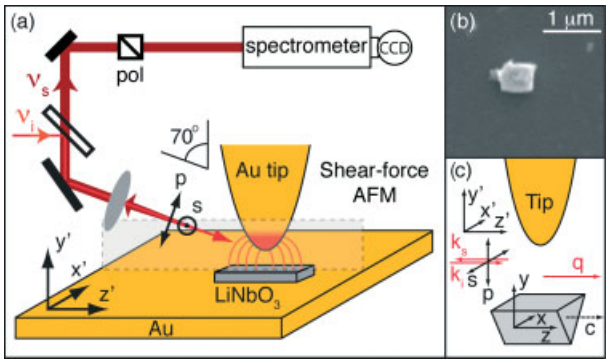

Figure 2. (a) Schematic of the side-illumination TERS setup using electrochemically etched Au tips. Tip–sample distance is controlled by use of shear-force feedback. The incident light ($\lambda = 632.8$ nm) is focused using a long-working-distance objective onto the tip–sample gap with near-grazing incidence ($\theta = 70^{\circ}$). The backscattered Raman signal is collected through the same objective, spectrally filtered with a long-pass Raman filter, and detected using a grating spectrometer with a N_2(l)-cooled CCD camera. (b) SEM micrograph of a $LiNbO_3$ nanocrystal prepared by powdering bulk $LiNbO_3$ crystal. Sizes of crystallites are found to be ≤ 1 µm. (c) Illustration of the geometry used for tip-enhanced Raman spectra with the phonon propagation direction as indicated. In all cases x, y, and z refer to the crystal coordinates, with z oriented along the optical axis, while x', y', and z' refer to the fixed lab frame.

delocalization of the vibrational and electronic wavefunctions and the associated weaker electron–phonon coupling per unit volume in crystalline materials leading to a smaller Raman cross section for solids.[38] In addition, large bandgaps of dielectric materials contrast many molecular systems that can benefit from resonant or near-resonant Raman cross sections in the visible region. Furthermore, in molecular studies, the use of a metallic substrate can give rise to strong tip–sample coupling to produce a further field enhancement over that of the freestanding tip.[11] For nanocrystals of thicknesses even as small as a few tens of nanometers, this effect is greatly diminished. As a consequence, a comparatively weak signal is expected for crystalline materials.

The TERS signal expected from crystalline structures can be quantitatively derived from an analysis of the Raman scattering cross section. The differential Raman scattering cross section given by $d\sigma/d\Omega = N_s/N_i$, where N_s is the number of photons scattered into a solid angle $d\Omega$, and N_i the incident photon flux. For molecular systems $d\sigma/d\Omega$ is typically given by (area/molecule·steradian). For solids σ is given in a volume-normalized form.[39] For crystalline materials, typical values for $d\sigma/d\Omega$ range from 10^{-8} to $\times 10^{-5}$/cm·sr.[30,32,40] For molecular systems, $d\sigma/d\Omega$ can vary from 10^{-30} for nonresonant excitation up to 10^{-26} cm^2/molecule·sr for the resonant case.[41] In order to obtain an effective scattering cross section for solids, we multiply the volume-normalized value by the scattering volume. Therefore, to match the Raman cross section of a single resonant molecule, a bulk crystal volume of 1 to 1000 nm^3 must be probed. With an effective near-field tip-enhanced probe volume of ~1000 nm^3 as given to first order by the spatial extent of the enhanced field region of a tip with ~10 nm apex radius, a comparatively large crystal volume is probed. However, the limited field enhancement resulting from the absence of strong tip–sample coupling[42] requires crystalline materials with large Raman scattering cross sections to obtain appreciable TERS signals. The absence of bleaching, which remains a concern for organic molecular systems[11,43] allows the use of a higher laser fluence and longer signal acquisition times to compensate for the smaller scattering cross sections. We will revisit this issue after presenting the experimental results.

Following these general considerations, we will illustrate the use of the Raman selection rules in the far-field, and demonstrate TERS from $LiNbO_3$ nanostructures.

Experimental

Far-field Raman spectra were acquired from a single-crystal z-cut $LiNbO_3$ wafer (Crystal Technology Inc.) using confocal epi-illumination and detection with a numerical aperture (NA) = 0.1 objective (Olympus), in an experimental geometry as shown in Fig. 1(b). Our experimental near-field setup is based on a home-built scattering-type scanning near-field optical microscope (*s*-SNOM) as shown in Fig. 2(a). Side-on illumination is used, with the incident light focused by a long-working-distance objective (Nikon, NA = 0.35, working distance = 20.5 mm) onto the tip–sample gap with a laser fluence of $\sim 3 \times 10^4$ W/cm^2. The backscattered Raman signal is collected through the same objective. In all cases, a He–Ne excitation source ($\lambda = 632.8$ nm) is used. The signal is spectrally filtered by a long-pass filter with a ~200 cm^{-1} cutoff. The filtered signal is detected by a grating spectrometer with a N_2(l)-cooled CCD camera. Incident and detected polarization were set using a $\lambda/2$ wave plate and a polarizer, respectively. Tips are prepared from Au wire ($\phi = 125$ µm), applying a previously descibed electrochemical etching technique,[44] and mounted on the quartz tuning fork of a shear-force atomic force microscope (AFM). $LiNbO_3$ crystallites are prepared by manually grinding a bulk crystal to crystallites of size ≤ 1 µm, and are dispersed onto an evaporated Au substrate from ethanol by drop-casting. An electron micrograph of a typical crystallite is shown in Fig. 2(b). Independent characterization of the $LiNbO_3$ crystallites is performed by micro-Raman spectroscopy using an NA = 0.8 objective.

Results and Discussion

For $LiNbO_3$, the Raman tensors of the C_{3v} trigonal crystal class are given by:[39]

$$\mathbf{A_1}(z) = \begin{pmatrix} a & 0 & 0 \\ 0 & a & 0 \\ 0 & 0 & b \end{pmatrix}, \mathbf{E}(x) = \begin{pmatrix} c & 0 & d \\ 0 & -c & 0 \\ d & 0 & 0 \end{pmatrix},$$
$$\mathbf{E}(y) = \begin{pmatrix} 0 & -c & 0 \\ -c & 0 & d \\ 0 & d & 0 \end{pmatrix}.$$

Here x, y, and z are the phonon polarization directions for the respective modes along the corresponding crystallographic axes. The use of selection rules in far-field Raman scattering is illustrated in Fig. 3, showing the Raman spectra acquired from bulk $LiNbO_3$ in the scattering configurations as indicated (Porto notation, from left to right: incident k-vector direction, incident polarization, detected polarization, and scattered k-vector direction). In all cases, the z-axis corresponds to the optical c-axis. We use x, y, and z to denote the crystal axes, and x', y', and z' for the lab frame.

Peak positions are in good agreement with and are assigned according to previous studies of $LiNbO_3$.[34,45,46] As can be seen from applying the Raman selection rules from above, the spectrally distinct subset of high-wavenumber modes are the A_1^{TO} at 630 cm^{-1} $(x(z,z)\bar{x}$, $y(z,z)\bar{y}$, and $y(x,x)\bar{y})$, E^{TO} at 576 cm^{-1} $(y(z,x)\bar{y}$ and $x(z,y)\bar{x})$, A_1^{LO} 871 cm^{-1} $(z(y,y)\bar{z})$, and the E^{LO} 877 cm^{-1} $(x(y,y)\bar{x})$

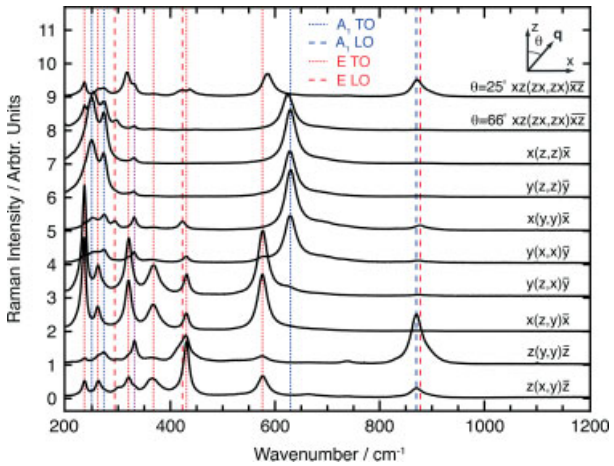

Figure 3. Far-field Raman spectra of $LiNbO_3$ bulk crystal for different scattering configurations (vertically offset for clarity, in Porto notation). Oblique-incidence spectra showing quasi-modes are shown with the phonon propagation direction at an angle θ with respect to the z-axis as calculated from the high-wavenumber TO mode spectral position as discussed in the text.

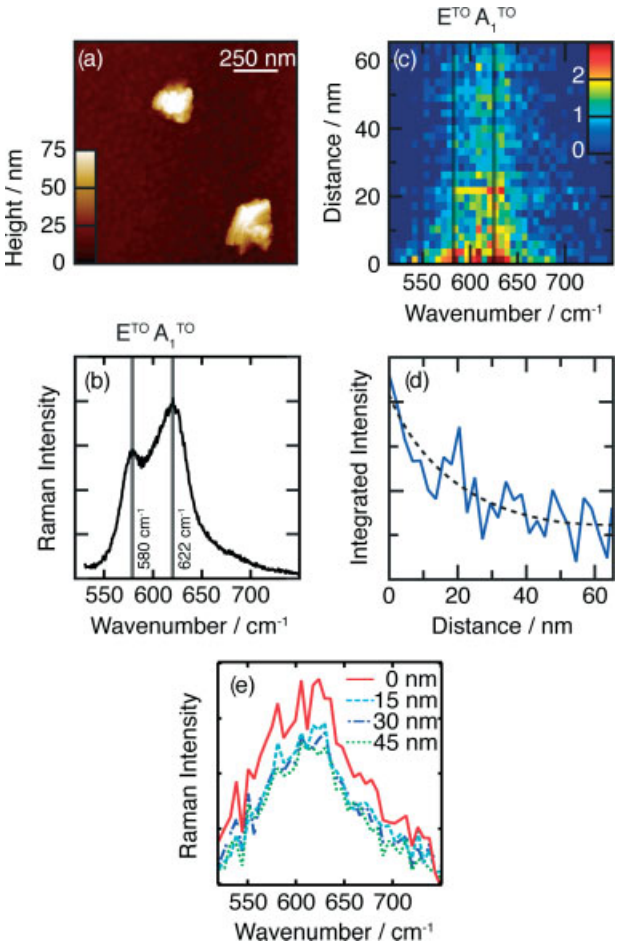

Figure 4. (a) Noncontact-AFM topography of typical $LiNbO_3$ nanocrystals prepared by grinding a bulk crystal. The nanoscale roughness of the Au substrate is characteristic of the evaporated Au deposition. (b) Far-field Raman spectrum obtained from a small ensemble of $LiNbO_3$ nanocrystals. (c) Distance dependence of the background-subtracted TERS signal intensity with the tip approaching a $LiNbO_3$ crystal. The integrated TERS intensity from (c) is shown in (d) with the dashed line as a guide to the eye. The incrase in signal at distances less than ~30 nm is correlated with the tip-apex radius and demonstrates the near-field character of the signal. (e) Four spectra at various tip–nanocrystal distances obtained by averaging seven adjacent spectra in (c), with the height indicated corresponding to the spectrum of closest tip–sample approach. The increased spectral resolution in (b) is due to a higher resolution grating and the narrower spectrometer slitwidth. The signal variation in (e) is due to photon counting noise and systematic variations in CCD detector pixel sensitivity.

mode. The observation of the A_1^{LO} mode in the forbidden $z(x,y)\bar{z}$ geometry is attributed to the k-vector distribution at the focus of the objective used. An analogous description and assignment of the low-wavenumber modes is readily possible.

Also seen are two examples of Raman spectra acquired with the phonon propagating at an angle θ with respect to the z-axis. From the peak positions of 622 and 586 cm^{-1} modes, the phonon propagation can be calculated to be at an angle of 66° and 25°, respectively, in excellent agreement with the experimentally set angles. This peak analysis thus illustrates the general capability of Raman scattering to determine the crystallographic orientation with respect to the lab frame. Likewise, the extension to TERS will allow crystal indexing at the nanoscale using the far-field spectra as reference.

TERS results from $LiNbO_3$ nanocrystals are shown in Fig. 4. Panel (a) shows the noncontact-AFM topography of two single-crystalline nanocrystals. The irregular shape is a result of the mechanical preparation procedure. Figure 4(b) shows the far-field Raman spectrum of a small ensemble of these nanocrystals deposited on a Si substrate. As expected, the A_1^{TO} peak is broadened and shifted to a lower wavenumber of 622 cm^{-1}. This can be attributed to a combination of two factors. First, as a result of probing randomly oriented crystallites, the quasi TO mode comes into effect. If we spatially average over all possible angles between the z-axis and the phonon propagation direction for a randomly oriented crystal, we find $\cos(\theta) = 1/\pi$. Using this value to calculate the wavenumber of the quasi TO mode, we expect an average of 625 cm^{-1}. This is in good agreement with the observed peak position, with the deviation likely to be due to an anisotropic distribution of the small particle ensemble probed. Second, the additional broadening results from the nanostructured surface of the crystallites, causing localized phonon confinement in the crystal and resulting in a reduced wavenumber of the Raman peak as well as broadening.[47]

Panel (c) of Fig. 4 shows the spectrally resolved TERS signal on approaching a nanocrystal after background subtraction. All spectra were acquired with incident p-polarization and unpolarized detection using an acquisition time of 20 s. The corresponding tip–sample distance dependence of the integrated spectra from (c) are shown in panel (d). A increase in the TERS intensity is seen for distances of <30 nm, correlated with the tip apex radius,[11] as expected, which is indicative of the near-field signature. Panel (e) shows four spectra at different tip–nanocrystal distances obtained by averaging seven adjacent spectra in (c), with the distance indicated corresponding to the spectrum of closest approach of the seven averaged spectra. The Raman signal as seen for larger distances is due to the far-field response from nanocrystals located within the far-field focus. The higher spectral resolution in the far-field data (b) is due to a higher resolution grating and the narrower spectrometer slitwidth used.

Although both the A_1^{TO} and E^{TO} appear appear to be enhanced in the near-field, the signal-to-noise ratio prevents a definitive assignment. For the following, we assume an enhancement of the A_1^{TO} mode with no enhancement for the E^{TO} mode for illustration

purposes only. The observation of the A_1^{TO} mode indicates a phonon propagation direction in the *x*-*y* plane. The absence of the E^{TO} mode could be attributed to either (1) an orientation of the *z*-axis along the polarization direction, or (2) $\mathbf{q} \parallel x$. While the latter case would allow for the E^{LO} mode, this is a weak mode, and given the low signal levels in the TERS experiment we do not expect it to be observable. This allows us to conclude that the crystallite is oriented with the phonon propagation direction in the *x*-*y* plane, and either the *y* or *z* axis to be oriented along the tip axis. In the above discussion, it was also assumed on the basis of the only moderate signal of the A_1^{TO} mode, corresponding to the $p_{in}p_{out}$ configuration, that modes under $p_{in}s_{out}$ would not be observable.

In order to obtain a quantitative understanding of the field enhancement in polar phonon TERS, we consider the scattering cross section of $LiNbO_3$. The large scattering cross section for the 630 cm^{-1} A_1^{TO} mode is reported to be 10^{-5} /cm·sr.[30] Thus, probing 1 nm^3 of $LiNbO_3$ would correspond to a scattering cross section of 10^{-26} cm^2/sr, slightly smaller than one dye molecule under resonant excitation conditions.[41] If we assume an effective near-field probe volume of 1000 nm^3, a scattering cross section of 10^{-23} cm^2/sr is obtained. With our laser fluence of $\sim 3 \times 10^4$ W/cm^2, this corresponds to 10^{23} photons/s, and as such we expect one Raman scattered photon per second per steradian in the absence of field enhancement. If we consider the detection of ~200 near-field Raman scattered photons per second, taking into account the NA of our objective and losses in the detection, this corresponds to a Raman enhancement on the order of $10^3 - 10^4$.

Assuming the Raman enhancement $\propto |F_p|^4$, this is consistent with typical field enhancement values for a freestanding tip on the order of ~10[10,48] (and Ref. [49] and references therein). From the TERS Raman signal observed, it can be seen that the lack of plasmonic tip–sample coupling, which can account for an additional field enhancement of ~10,[11,42] is partially offset by the ~1000 nm^3 crystal volume probed by the near-field as well as the longer acquisition times used.

For maximum sensitivity, emphasis must be placed on tip fabrication and design. To obtain sufficient tip enhancement, both the pump and Raman scattered light should overlap spectrally with the plasmon mode of the tip, as can readily be the case for relatively small Raman shifts (i.e. <1000 cm^{-1}). Furthermore, the tip sharpness is of critical importance to obtain maximum enhancement. However, tip fabrication is still mostly an empirical process with large variability, and obtaining specific resonances, homogeneous lineshape, and high Raman enhancement factors has remained challenging.

In addition, several effects have to be considered associated with the fact that the Raman excitation is driven by a spatially inhomogeneous near-field distribution associated with the tip apex. So-called gradient field Raman effects may arise due to the resulting strong field gradients.[50] They can fundamentally change the selection rules and render previously Raman inactive modes visible.[11,51] However, this effect has only been observed for very high Raman enhancement ($>10^9$)[11] and can be neglected for the level of Raman enhancement relevant here. Furthermore, the tip-enhanced near-field contains electric field components both longitudinal and transverse with respect to the tip axis for both principal polarization orientations.[52] As a consequence, a depolarization of the near-field Raman signal can result,[17,18,53] leading to a relaxation of the far-field selection rules. However, with $F_p > F_s$, this effect is generally weak for symmetric tips,[52] and may be further minimized through the use of sharp tips of regular shape and high aspect ratio.[54]

The TERS analysis for the specific example discussed above for a given nanocrystal orientation can be generalized to provide a full selection rule table for TERS. The Raman modes expected for $LiNbO_3$ crystals of different crystal orientations in the TERS geometry are illustrated in Table I under the experimental geometry as shown in Fig. 1(c). With the shallow angle of incidence of the experimental backscattering geometry, the incident and scattered *k*-vectors can be approximated as being oriented in the sample plane, neglecting out-of-plane *k*-vector components.

Table 1. TERS selection rules for trigonal $LiNbO_3$ with one of the principal axes oriented parallel to the incident and scattered light

$q = k_i - k_s$	mode	$k_i(e_i, e_s)k_s$	I_{TERS}	Orientation
$\mathbf{q} \parallel z$	A_1^{LO}	$z(y,y)\bar{z} = p_{in}p_{out}$	$\propto \lvert a_{LO}\rvert^2 F_{pp}^2$	z'
"	E^{TO}	$z(y,y)\bar{z} = p_{in}p_{out}$	$\propto \lvert c_{TO}\rvert^2 F_{pp}^2$	"
"	E^{TO}	$z(y,x)\bar{z} = p_{in}s_{out}$	$\propto \lvert c_{TO}\rvert^2 F_{sp}^2$	"
$\mathbf{q} \parallel x$	A_1^{TO}	$x(z,z)\bar{x} = p_{in}p_{out}$	$\propto \lvert b_{TO}\rvert^2 F_{pp}^2$	y'
"	E^{TO}	$x(z,y)\bar{x} = p_{in}s_{out}$	$\propto \lvert d_{TO}\rvert^2 F_{sp}^2$	"
$\mathbf{q} \parallel y$	A_1^{TO}	$y(x,x)\bar{y} = p_{in}p_{out}$	$\propto \lvert a_{TO}\rvert^2 F_{pp}^2$	x'
"	E^{TO}	$y(x,x)\bar{y} = p_{in}p_{out}$	$\propto \lvert c_{TO}\rvert^2 F_{pp}^2$	"
"	E^{TO}	$y(x,z)\bar{y} = p_{in}s_{out}$	$\propto \lvert d_{TO}\rvert^2 F_{sp}^2$	"
$\mathbf{q} \parallel xz$	Q TO	$xz(y,y)\overline{xz} = p_{in}p_{out}$	$\propto (\lvert a_{TO}\rvert^2 + \lvert c_{TO}\rvert^2) F_{pp}^2$	zx'
"	Q LO	$xz(y,y)\overline{xz} = p_{in}p_{out}$	$\propto (\lvert a_{LO}\rvert^2 + \lvert c_{LO}\rvert^2) F_{pp}^2$	zx'
"	E^{TO}	$xz(y,zx)\overline{xz} = p_{in}s_{out}$	$\propto \lvert d_{TO} - c_{TO}\rvert^2 F_{sp}^2$	zx'
$\mathbf{q} \parallel xy$	A_1^{TO}	$xy(z,z)\overline{xy} = p_{in}p_{out}$	$\propto \lvert a_{TO}\rvert^2 F_{pp}^2$	y'
"	E^{TO}	$xy(z,yx)\overline{xy} = p_{in}s_{out}$	$\propto \lvert d_{TO}\rvert^2 F_{sp}^2$	y'
"	E^{LO}	$xy(z,yx)\overline{xy} = p_{in}s_{out}$	$\propto \lvert d_{LO}\rvert^2 F_{sp}^2$	y'

For each domain, the crystal coordinates are rotated to reflect the change in ferroelectric orientation (i.e. $c \parallel z$). Contributions under the weakly enhanced $s_{in}s_{out}$ configuration are neglected. Furthermore, as a consequence of the symmetric Raman tensors, for the cross-polarized configuration, only the p_{in} configuration is considered (i.e. $p_{in}s_{out} \simeq s_{in}p_{out}$). The orientation describes the *z*-axis alignment along one of the fixed axes in the lab frame as shown in Fig. 1a. Q denotes a quasi-mode as discussed in the text.

Furthermore, we assume the sample to be oriented either with one of the principal axes oriented parallel to the phonon propagation direction or at a 45° angle. Also, as a result of the symmetry selectivity of the tip enhancement, phonon modes observed under the weakly enhanced $s_{in}s_{out}$ are neglected. As a consequence of the symmetric Raman tensors, for the cross-polarized configuration, only the p_{in} configuration is considered (i.e. $p_{in}s_{out} \simeq s_{in}p_{out}$). These assumptions are made for illustration purposes, and the selection rules can easily be generalized for any TERS scattering geometry.

For our geometry, the A_1 mode may be observed for all crystalline orientations in the strongly enhanced $p_{in}p_{out}$ polarization configuration. However, it can be seen that the case of $\boldsymbol{q} \parallel z$ is easily distinguishable from other crystalline orientations with the A_1^{LO} mode being excited, while silent for all other orientations, which would in turn manifest themselves in the observation of the A_1^{TO} mode. The $\boldsymbol{q} \parallel x$ and $\boldsymbol{q} \parallel y$ cases may be distinguished by the observation or lack of the E^{TO} mode in the $p_{in}p_{out}$ configuration. However, for the crystal oriented along the y' coordinate, the observation of the E^{LO} mode under $p_{in}p_{out}$ is indicative of the orientation of the y-axis along the polarization direction. For oblique incidence, Q denotes a quasi-mode. In analogy to the far-field case, the Raman shift of the quasi-modes will allow the determination of the angle between the propagation direction and the z-axis and thus the crystallographic orientation.

While this approach is generally applicable, for bulk samples, complications can arise due to the far-field background. Assuming sufficient enhancement to obtain appreciable near-field to far-field contrast (which will depend on material scattering cross section, far-field focus size, and material transparency), the characteristics of the background can be established through distance-dependent measurements. With the far-field response expected to remain constant as the signal average over an extended sample area, background subtraction may be performed to obtain the near-field signature of the sample in the region of interest.

As in the far-field case, it can be seen from this discussion that the unique properties of polar mode scattering can yield information about the crystalline orientation not available from nonpolar modes. As such, careful consideration of the phonon propagation direction is critical. Furthermore, for optimum TERS spectra from crystalline materials, an emphasis must be placed on tip fabrication in order to maximize field enhancement and preserve the purity of the incident pump and scattered Raman polarization.

Conclusion and Outlook

In summary, we have outlined the application of TERS to the study of crystalline nanostructures, proposing the use of the symmetry selectivity of the Raman response to determine crystallographic orientation. The intrinsic Raman selection rules are discussed, including the use of the Raman tensor, momentum conservation for polar phonon modes, and the use of quasi-modes. These selection rules are superimposed with the symmetry consideration of the polarization selective enhancement of the plasmonic scanning probe tip to describe phonon TERS. Far-field Raman spectra from $LiNbO_3$ are presented to illustrate the Raman selection rules, and near-field results from $LiNbO_3$ nanocrystals are shown. The approach is generally applicable to most crystal structures exhibiting polar phonon modes with the notable exception of the highly complex triclinic crystal class, with details for a given crystal depending on the scattering cross sections and the spectral separation of individual modes. Taking full advantage of this capability will require knowledge of the polarization enhancement and scattering tensor of the tip, which is presently still difficult given the challenges associated with the reproducible fabrication of tips with defined plasmon resonant and scattering behavior. Nevertheless, the capability to probe crystal symmetry, in combination with the chemical specificity inherent to Raman scattering, as shown in this work, may position TERS as a powerful tool for the nanoscale analysis of crystalline materials including optical nanocrystallography.

Acknowledgements

S. Berweger acknowledges support from the University of Washington Center for Nanotechnology with funding from NSF-IGERT. Funding from the National Science Foundation (NSF CAREER grant CHE 0748226) is gratefully acknowledged. The authors would also like to thank the University of Washington Center for Nanotechnology User Facility for support, Prof. Antao Chen for the $LiNbO_3$ crystals, and Prof. Peter Yu for helpful discussions.

References

[1] P. Yu, M. Cardona, *Fundamentals of Semiconductors*, Springer: Berlin, **2005**.
[2] M. Cardona (ed.), *Light Scattering in Solids I*, Springer: Berlin, **1983**.
[3] F. Cerdeira, C. J. Buchenauer, F. H. Pollak, M. Cardona, *Phys. Rev. B* **1972**, *5*, 580.
[4] R. C. C. Leite, J. F. Scott, T. C. Damen, *Phys. Rev. Lett.* **1969**, *22*, 780.
[5] A. Mooradian, G. B. Wright, *Solid State Commun.* **1966**, *4*, 431.
[6] P. A. Fleury, J. M. Worlock, *Phys. Rev.* **1968**, *174*, 613.
[7] H. Taniguchi, M. Itoh, T. Yagi, *Phys. Rev. Lett.* **2007**, *99*, 017 602.
[8] P. L. Lagos, R. Z. Hermans, N. Velasco, G. Tarrach, F. Schlaphor, C. Loppacher, L. M. Eng, *Surf. Sci.* **2003**, *532*, 493.
[9] Z. Li, C. M. Foster, X.-H. Dai, X.-Z. Xu, S.-K. Chan, D. J. Lam, *J. Appl. Phys.* **1992**, *71*, 4481.
[10] A. Hartschuh, E. J. Sanchez, X. S. Xie, L. Novotny, *Phys. Rev. Lett.* **2003**, *90*, 095 503.
[11] C. C. Neacsu, J. Dreyer, N. Behr, M. B. Raschke, *Phys. Rev. B* **2006**, *73*, 193 406.
[12] J. Steidtner, B. Pettinger, *Phys. Rev. Lett.* **2008**, *100*, 236 101.
[13] W. Zhang, B. S. Yeo, T. Schmid, R. Zenobi, *J. Phys. Chem. C* **2007**, *111*, 1733.
[14] N. Anderson, A. Hartschuh, L. Novotny, *Nano Lett.* **2007**, *7*, 577.
[15] E. Bailo, V. Deckert, *Angew. Chem. Int. Ed.* **2008**, *47*, 1658.
[16] T. Ichimura, H. Watanabe, Y. Morita, P. Verma, S. Kawata, Y. Inouye, *J. Phys. Chem. C* **2007**, *111*, 9460.
[17] C. C. Neacsu, S. Berweger, M. B. Raschke, *NanoBiotechnol.* **2009**, *3*, 172.
[18] E. Bailo, V. Deckert, *Chem. Soc. Rev.* **2008**, *37*, 921.
[19] A. Hartschuh, *Angew. Chem. Int. Ed.* **2008**, *47*, 8178.
[20] R. Ossikovski, Q. Nguyen, G. Picardi, *Phys. Rev. B* **2007**, *75*, 045412.
[21] M. Motahashi, N. Hayazawa, A. Tarun, S. Kawata, *J. Appl. Phys.* **2008**, *103*, 034309.
[22] W. Hayes, R. Loudon, *Scattering of Light by Crystals*, Dover Publications: Mineola, NY **1978**.
[23] S. Berweger, C. C. Neacsu, Y. Mao, H. Zhou, S. S. Wong, M. B. Raschke, *Nat. Nanotechnol.* **2009**, *4*, 496.
[24] M. Lines, A. Glass, *Principles and Applications of Ferroelectric and Related Materials*, Oxford University Press: Oxford, **2001**.
[25] R. W. Boyd, *Nonlinear Optics*, Elsevier Science: San Diego, CA **2003**.
[26] D. Janner, D. Tulli, M. Belmonte, V. Pruneri, *J. Opt. Soc. Am. A* **2008**, *10*, 104003.
[27] E. L. Wooten, K. M. Kissa, A. Yi-Yan, E. J. Murphy, D. A. Lafaw, P. F. Hallemaier, D. Maack, D. V. Attanasio, D. J. Fritz, G. J. McBrien D. E. Bossi, *IEEE J. Sel. Top. Quantum Electron.* **2000**, *6*, 69.
[28] G. D. Miller, R. G. Batchko, W. M. Tulloch, D. R. Weise, M. M. Fejer, R. L. Byer, *Opt. Lett.* **1997**, *22*, 1834.
[29] L. E. Myers, R. C. Eckardt, M. M. Fejer, R. L. Byer, W. R. Bosenberg, J. W. Pierce, *J. Opt. Soc. Am. B* **1995**, *12*, 2102.

[30] W. D. Johnston, I. P. Kaminow, *Phys. Rev.* **1968**, *168*, 1045.
[31] T. T. Basiev, A. A. Sobol, P. G. Zverev, L. I. Ivleva, V. V. Osiko, R. C. Powell, *Opt. Mater.* **1999**, *11*, 307.
[32] D. L. C. A. Arguello, S. P. S. Porto, *Phys. Rev.* **1969**, *181*, 1351.
[33] R. Loudon, *Adv. Phys.* **1964**, *13*, 423.
[34] R. F. Schaufele, M. J. Weber, *Phys. Rev.* **1966**, *152*, 705.
[35] C. C. Neacsu, G. A. Steudle, M. B. Raschke, *Appl. Phys. B* **2005**, *80*, 295.
[36] E. C. Le Ru, J. Grand, N. Felidj, J. Aubard, G. Levi, A. Hohenau, J. R. Krenn, E. Blackie, P. G. Etchegoin, *J. Phys. Chem. C* **2008**, *112*, 8117.
[37] Y. R. Shen, *The Principles of Nonlinear Optics*, John Wiley & Sons: Academic Press, Burlington, MA **1984**.
[38] Y.-M. Chang, L. Xu, H. Tom, *Chem. Phys.* **2000**, *251*, 283.
[39] H. Kuzmany, *Solid-State Spectroscopy*, Springer: Berlin, **1998**.
[40] J. Ralston, R. Chang, *Phys. Rev. B* **1970**, *2*, 1858.
[41] E. Le Ru, E. Blackie, M. Meyer, P. Etchegoin, *J. Phys. Chem. C* **2007**, *111*, 13794.
[42] N. Behr, M. B. Raschke, *J. Phys. Chem. C* **2008**, *112*, 3766.
[43] B. Pettinger, B. Ren, G. Picardi, R. Schuster, G. Ertl, *J. Raman Spectrosc.* **2005**, *36*, 541.
[44] B. Ren, G. Picardi, B. Pettinger, *Rev. Sci. Instrum.* **2004**, *75*, 837.
[45] R. Claus, G. Borstel, E. Wiesendanger, L. Steffan, *Phys. Rev. B* **1972**, *6*, 4878.
[46] A. S. Barker Jr, R. Loudon, *Phys. Rev.* **1967**, *158*, 433.
[47] H. Richter, Z. P. Wang, L. Ley, *Solid State Commun.* **1981**, *39*, 625.
[48] R. M. Roth, N. C. Panoiu, M. M. Adams, R. M. Osgood, C. C. Neacsu, M. B. Raschke, *Opt. Express* **2006**, *14*, 2921.
[49] D. Roy, J. Wang, C. Williams, *J. Appl. Phys.* **2009**, *105*, 013530.
[50] E. J. Ayars, H. D. Hallen, C. L. Jahncke, *Phys. Rev. Lett.* **2000**, *85*, 4180.
[51] C. C. Neacsu, J. Dreyer, N. Behr, M. B. Raschke, *Phys. Rev. B* **2007**, *75*, 236402 (pages 5).
[52] A. L. Demming, F. Festy, D. Richards, *J. Chem. Phys.* **2005**, *122*, 184716.
[53] T. T. Vladimir Poborchii, T. Kanayama, *Jpn J. Appl. Phys.* **2005**, *44*, 202.
[54] P. Gucciardi, M. Lopes, R. Deturche, C. Julien, D. Barchiesi, M. L. de la Chapelle, *Nanotechnology* **2008**, *19*, 215702.

